Engineering Structures 245 (2021) 112964

Contents lists available at ScienceDirect

Engineering Structures

journal homepage: www.elsevier.com/locate/engstruct

A stress-weighted ductile fracture model for steel subjected to Ultra Low Cycle Fatigue

Christopher Smith [a,*], Andy Ziccarelli [b], Masao Terashima [b], Amit Kanvinde [c,*], Gregory Deierlein [b]

[a] Berkshire Hathaway Specialty Insurance, USA
[b] Department of Civil and Environmental Engineering, Stanford University, USA
[c] Department of Civil and Environmental Engineering, University of California, Davis, USA

ARTICLE INFO

Keywords:
Ductile fracture
Ultra Low Cycle Fatigue
Structural steel

ABSTRACT

A new criterion is proposed to simulate the initiation of ductile fracture due to Ultra-Low Cycle Fatigue (ULCF). Building on previous research, the new fracture criterion broadens the scope of ULCF models to account for a broader range of multi-axial stress and strain states that may be encountered in steel structures. The model formulation, supported by observations from finite element plasticity simulations of void growth and fractographic analyses of fracture surfaces, describes damage accumulation as a function of plastic strain, stress triaxiality, and the Lode stress parameter. The damage rate model is integrated over arbitrary cyclic loading histories of local strains and stresses to predict ULCF fracture. The proposed criterion (termed the Stress Weighted Ductile Fracture Model – SWDFM) is supported by a series of 66 coupon scale experiments on two grades of low-carbon structural steel (A572 and A36). These tests interrogate a range of positive and negative stress triaxiality with absolute values between 0.1 and 1.6, Lode stress parameters between 0 and 1, and monotonic and cyclic loading histories. The SWDFM criterion, which requires the calibration of only two material parameters for the materials investigated in this study, is evaluated against the experimental test data using an average-error assessment as well as a cross-validation analysis. Three other ULCF rupture criteria are similarly assessed and compared. The SWDFM is shown to accurately predict ULCF initiation over a wide range of stress states and loading histories, suggesting that the model represents well the micro-mechanical mechanisms of ULCF.

1. Introduction

Ductile fracture in metals is a well-studied phenomenon, including landmark experimental tests by Bridgman [1] and theoretical studies to understand the underlying mechanisms and proposed predictive models to simulate ductile fracture (e.g., McClintock [2]; Rice and Tracey [3]). Since then, many studies, including prior work by the authors (e.g., Kanvinde and Deierlein [4,5]), have extended, refined and integrated the early studies with continuum finite element methods to characterize ductile fracture initiation under monotonic and cyclic loading. However, most of the prior studies have been limited to a relatively narrow range of stress–strain states and loading conditions (e.g., number and amplitude of cycles), relative to conditions that can arise in practical design of steel structures under earthquakes and other extreme loads. In this paper, a newly proposed model is described for ductile fracture of low-carbon (mild) steel, which is validated against test data for a wide range of monotonic and cyclic loading conditions with large plastic strains and multi-axial stress states.

While there is broad agreement regarding the micromechanisms of ductile fracture in low-carbon steels, i.e., growth and coalescence of microvoids that nucleate around inclusions within the ferrite-pearlite microstructure and result in dimpled fracture surfaces (illustrated in Fig. 1), the published literature reveals a large number of competing models that have been proposed to simulate ductile fracture. The focus in this paper is on ductile fracture in structural steel subjected to high-strain Ultra-Low Cycle Fatigue (ULCF) with cyclic or random loading histories and fewer than 40 cycles under a wide range of stress states. In such conditions, conventional fracture mechanics (Linear Elastic or Elastic Plastic – Anderson [6]) is not applicable, and “local” or micromechanical fracture criteria (Besson et al. [7]) become necessary. These

---

* Corresponding authors.
E-mail address: kanvinde@ucdavis.edu (A. Kanvinde).

https://doi.org/10.1016/j.engstruct.2021.112964
Received 11 November 2020; Received in revised form 10 June 2021; Accepted 6 August 2021

local fracture criteria are typically formulated as combinations of stress and strain histories up to critical values that trigger ductile crack initiation. These models can be broadly distinguished between "uncoupled," where the failure criterion is applied after the stress and strain fields of the continuum have been determined, or as "coupled", where the interaction of material damage with the surrounding stress–strain fields is explicitly simulated through modification of constitutive response (e.g., Gurson [8]). This paper addresses uncoupled models, which are more convenient to apply to simulate fracture initiation, requiring only the post-processing of stress–strain fields typically determined through continuum finite element simulations of the component or structure of interest.

In contrast to damage mechanics based fracture criteria that have focused on monotonic loading and been under development for over four decades (e.g., (Hancock and Mackenzie [9]; Rousselier [10]) criteria for ULCF fracture have been more recently developed, motivated by earthquake-induced fractures in buildings and other civil infrastructure. Recent work has also provided new focus on characterizing the critical plastic strain under low stress triaxiality (i.e., $T < 0.7$) and variable shear stress states, as characterized by the Lode parameter X. Triaxiality is defined as the ratio of the mean (hydrostatic) stress to the von Mises (deviatoric) stress, i.e., $T = (I_1/3)/\sqrt{3J_2}$, where I_1 and J_2 are the first and second invariants of the stress tensor, and deviatoric stress tensor respectively. The Lode parameter relates J_3, the third stress invariant, to J_2, i.e., $X = 3\sqrt{3}\cdot J_3/(2\cdot J_2^{3/2})$, distinguishing shear stress states ranging from axisymmetric ($X = \pm 1$) to plane strain ($X = 0$). Previously proposed models to simulate ULCF fracture include Kanvinde and Deierlein [4] and Kiran and Khandelwal [11], which consider dependence on triaxiality, and Wen and Mahmoud [12], which considers dependence on both triaxiality and Lode parameters. These models all feature a primary dependence of damage on accumulation by plastic strain, weighted by functions of T and X.

The above criteria are generally consistent and accurate within the scope of the datasets on which they are developed, often round notched bars with axisymmetric stress–strain conditions. Generally, this scope has focused on high T fracture because 1) high T significantly promotes void growth that can lead to ductile fracture, and 2) many structures contain geometric imperfections that give rise to strain localization and high T. Recognizing these points, modern design and detailing requirements for steel structures have been revised to avoid high stress triaxiality in areas where large plastic strains are expected during earthquakes and other extreme loading. These changes in design standards have given rise to the need for models that can better capture ULCF fracture in non-axisymmetric and low-triaxiality conditions.

The main objective of this paper is to propose and validate a new criterion for ductile fracture in structural steels, with the following features: (1) inclusion of the effects of both the Lode parameter and the stress triaxiality (X and T) over a wide range, (2) fewer calibration coefficients compared to other competing models, (3) validation against both new and previously published data from tests of low-carbon steel specimens under a range of monotonic and cyclic loading protocols, and (4) quantitative comparisons with other models. To this end, the paper synthesizes data from 66 tests of various coupon-scale specimen geometries for two structural steels, ASTM A572 and A36, and a along with supporting observations from a computational void cell model study, culminating in the development of a newly proposed Stress-Weighted Ductile Fracture Model (SWDFM). The SWDFM, and three previously published models, are calibrated and evaluated against finite element simulation results of the 66 tests.

2. Background: local rupture criteria for predicting ULCF in steel

Local rupture criteria arise from the observation that the damage driving the fracture process occurs with the accumulation of plastic strain, wherein the rate of accumulation depends on the local stress and strain state. These models are represented in the following generic form:

$$D = \int dD = \int_0^{\varepsilon_p} f(\widetilde{\sigma}, \widetilde{\varepsilon})\cdot d\varepsilon_p \geqslant 1 \tag{1}$$

where $f(\widetilde{\sigma}, \widetilde{\varepsilon})$ is a scalar function of the stress and strain tensors $\widetilde{\sigma}, \widetilde{\varepsilon}$ and $d\varepsilon_p = \sqrt{(2/3) \times d\varepsilon_p : d\varepsilon_p}$ is the incremental equivalent plastic strain. Ductile fracture is predicted to occur when the damage D equals unity. The function $f(\widetilde{\sigma}, \widetilde{\varepsilon})$, which modifies the instantaneous damage rate with respect to the plastic strain, represents the underlying fracture mechanism and the material properties. In some models, e.g., the Stress Modified Critical Strain – SMCS model (Hancock and Mackenzie [9]), the fracture criterion is pre-integrated to represent the critical plastic strain as a function of stress state, assuming that the stress state (and hence the damage rate) is relatively constant over the loading history. As will be demonstrated later, for lower triaxiality conditions, the evolution in the damage rate is significant. Therefore the focus in this paper is on path dependent models of the form in (1). The above criterion is applied locally within the continuum, often in conjunction with a characteristic length l^* to account for material sampling effects. The effect of l^* is significant when steep damage gradients are present, for example ahead of a sharp crack tip. This paper addresses only the fracture criterion based on test data from specimens with shallow damage gradients that are not sensitive to l^*. Once the fracture criterion is established, l^* can be determined from fractographic measurements (e.g., Kanvinde and Deierlein [5]) or calibration to data from tests with sharp cracks, such as compact tension specimens (Norris et al. [13]).

Previous fracture criteria have been developed as a best fit through test data, or through adaptations of analytical derivations for void

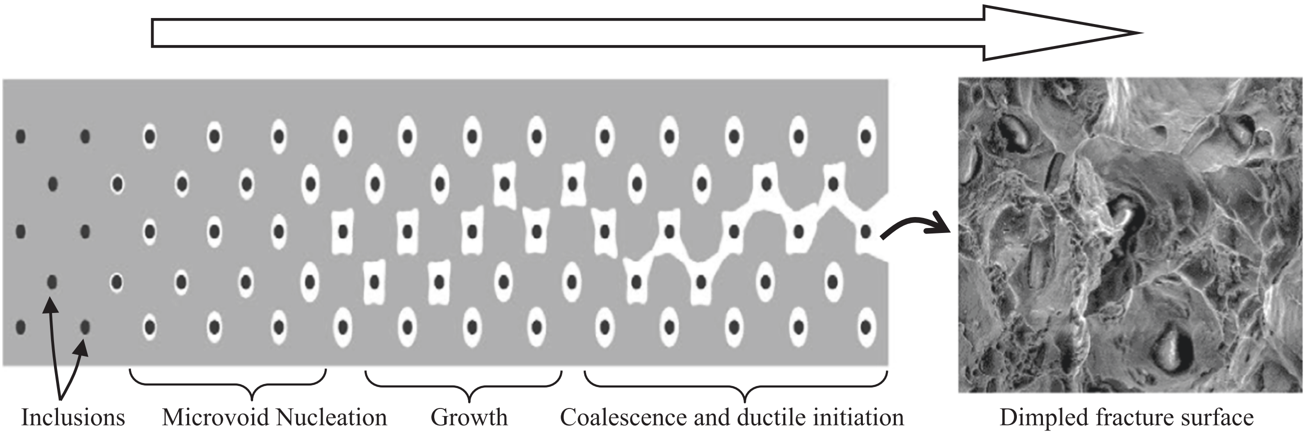

Fig. 1. Progression of micromechanical processes leading to ductile rupture in steel.

growth in elastoplastic continua. Notable among the latter is the derivation by Rice and Tracey [3] where the growth rate of spherical voids is described by a hyperbolic sine dependence (or the alternative exponential equivalent) of applied stress triaxiality and plastic strain:

$$\begin{aligned} dR_{void}/R_{void} &= 0.283\cdot[2sinh(1.5T)]\cdot d\varepsilon_p \\ &= 0.283[exp(1.5T) - exp(-1.5T)]\cdot d\varepsilon_p \end{aligned} \tag{2}$$

In the above equation, dR_{void}/R_{void} represents the incremental void growth, which is proportional to the incremental plastic strain $d\varepsilon_p$, wherein the proportionality is a strong function of the stress triaxiality T. The more commonly known form of this equation (termed the Void Growth Model – VGM, see Panontin and Sheppard [14]) is its approximation for high triaxiality (i.e., $T > 1$) cases where the hyperbolic sine approaches a single term exponential dependence. The integral form of this simplified relation can be written in terms of a critical damage parameter, D, as follows:

$$D = \int dD = \eta_{VGM} \times \int_0^{\varepsilon_p} exp(1.5T)\cdot d\varepsilon_p \geqslant 1 \tag{3}$$

where the term η_{VGM} is a material parameter.

The authors (Smith et al. [15]) previously reported a reanalysis of a theory and test data related to fracture under axisymmetric stress states – including CNT specimens, round bars, high pressure tension coupons tested by Bridgman [1]. This study is unique in the consideration of axisymmetric stress states triaxiality between −0.5 and 2, while also considering the significant effect of path dependence. For lower levels of stress triaxiality, the traditional VGM interpretation (3) is not valid, and a model consistent with the form of (2) is most appropriate. A further key implication of this study is the existence of a fracture cutoff (triaxiality below which fracture does not occur) at $T = 0$.

For ULCF under reversed cyclic loading, fractographic evidence (Kanvinde and Deierlein [12]) suggests that the micromechanisms of ULCF are similar to ductile fracture under monotonic loading (microvoid growth, collapse, and coalescence) as opposed to dislocation slip and decohesion mechanisms common to high cycle fatigue (Suresh [16]). Based on this observation, Kanvinde and Deierlein [5] extended the VGM to simulate ULCF fracture, which can occur to steel structures under earthquake loading. Termed the Cyclic Void Growth Model (CVGM), the rupture criterion may be defined as follows, where the subscript CVGM connotes the damage parameters that are unique to the cyclic model:

$$\begin{aligned} D_{CVGM} &= \int dD_{CVGM} \\ &= \eta_{CVGM}\left(\sum_{T\geqslant 0}\int exp(1.5|T|)\cdot d\varepsilon_p - \sum_{T<0}\int exp(1.5|T|)\cdot d\varepsilon_p\right) \\ &\quad \times e^{-\lambda_{CVGM}\cdot\varepsilon_c} \geqslant 1.0 \end{aligned} \tag{4}$$

In the CVGM damage is assumed to increase due to microvoid growth under plastic strains when $T \geq 0$ and reduce due to microvoid shrinkage when $T < 0$. The exponential decay term $e^{-\lambda_{CVGM}\cdot\varepsilon_c}$ accounts for the nonrecoverable damage during reversed cyclic loading, which occurs due to deterioration of the material matrix, where the term ε_c represents the

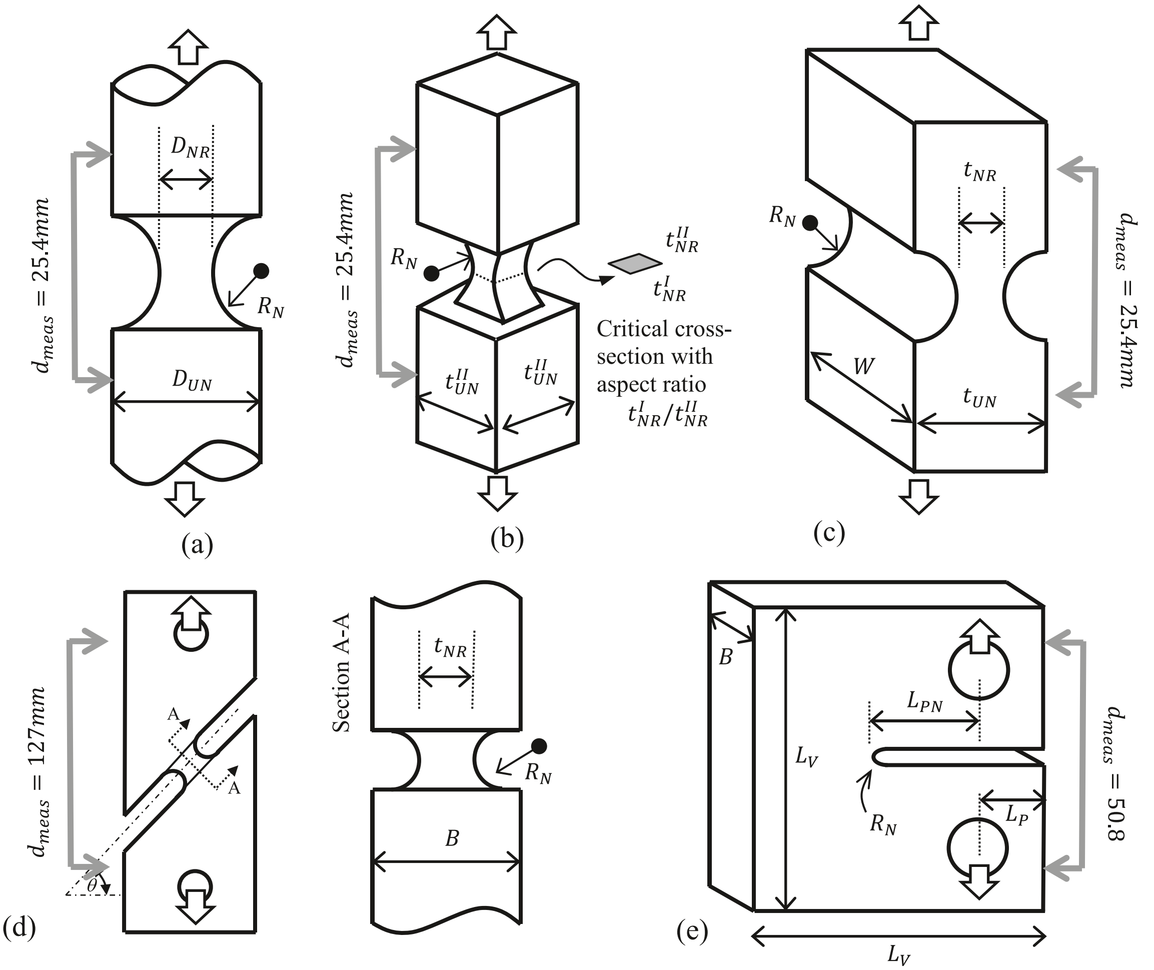

Fig. 2. Fracture specimens used in this study: (a) Circumferentially Notched Tensile – CNT, (b) Rectangular Notched – RN, (c) Grooved Plate – GP, (d) Inclined Notch – IN and (e) Blunt Notched – BN; *dmeas* indicates gage length for deformation measurement,

accumulated plastic strain during all preceding compressive cycles when $T < 0$ (Myers et al. [17]). The CVGM model includes two material parameters η_{CVGM} and λ_{CVGM} that can be calibrated from test data. The CVGM was developed from Circumferentially Notched Tension (CNT) specimens, which is shown in Fig. 2a, along with some alternative specimen configurations that will be discussed later. As shown in Fig. 3a, CNT specimens are limited to a specific range within the T-X stress space: axisymmetric ($X = 1$) and relatively high triaxiality ($T > 0.8$). Consequently, the CVGM is not presumed to be valid outside this range of stress states.

Kiran and Khandelwal [11] proposed an alternate fracture criterion (denoted KK) for ULCF, which is given by the following equation:

$$D_{KK} = \int dD_{KK} = \frac{1}{d_{cr,KK}}\left(\sum_{T\geqslant 0}\int a_{1,KK}|T|^{b_{1,KK}}d\varepsilon_p - \sum_{T<0}\int a_{2,KK}|T|^{b_{2,KK}}d\varepsilon_p\right)\geqslant 1.0 \tag{5}$$

Similar to the CVGM, the KK model divides the loading history into positive and negative regimes, based on triaxiality. However, it uses a power function of T instead of the exponential function to control damage accumulation (void growth), and it incorporates cyclic degradation through unequal values of material dependent parameters for damage accumulation in tension ($b_{1,KK}$, $a_{1,KK}$) versus compression ($a_{2,KK}$, $b_{2,KK}$). The term $d_{cr,KK}$ is a material dependent term that is based on the critical value of damage. Similar to the CVGM, the KK model is derived from the behavior of CNT specimens, and is not presumed valid for the broader range of stress states.

Wen and Mahmoud [12] developed a ductile fracture criterion for ULCF that incorporates low-triaxiality as well as nonproportional loading effects. This criterion (denoted WM) is given by the following equations:

$$D_{WM} = \int dD_{WM} = \int exp(c_{14,WM}\cdot\kappa)\cdot m_{WM}\cdot\left(\frac{\varepsilon_{pt}}{\varepsilon_f}\right)^{m_{WM}-1}\cdot\frac{d\varepsilon_p}{\varepsilon_f}\geqslant 1.0 \tag{6a}$$

where

$$\kappa = \int_0^{\varepsilon_p}\left[\frac{\sum_{i=1}^{3}\sum_{j=1}^{3}\sigma_{ij}}{\|\widetilde{\sigma}\|_1} - \frac{\sum_{i=1}^{3}\sum_{j=1}^{3}\alpha_{ij}}{\|\widetilde{\alpha}\|_1}\right]d\varepsilon_p \tag{6b}$$

$$\varepsilon_{pt} = \sqrt{(2/3)\bullet\varepsilon_p : \varepsilon_p} \tag{6c}$$

$$\varepsilon_f = c_{3,WM}\cdot exp\left(c_{4,WM}\times T\right)\cdot\left[cos\left(\frac{\pi}{6}\theta_{Lode}\right)\right]^{c_{5,WM}}\cdot\left[1 + c_{6,WM}(\chi - 0.5)\right] \tag{6d}$$

$$\chi = \frac{sin\left[\frac{\pi}{6}(1 - \theta_{Lode})\right]}{cos\left(\frac{\pi}{6}\theta_{Lode}\right)} \tag{6e}$$

In this model, the term $m_{WM}\cdot\left(\frac{\varepsilon_{pt}}{\varepsilon_f}\right)^{m_{WM}-1}$ in Eq. (6a) controls the nonlinearity in the rate of damage accumulation a function of the failure strain quantity ε_f, which is a function of T and the Lode angle $\theta_{Lode} = (1/3)\times arccos(X)$. Referring to Eq. (6d), the dependence on T is exponential, following the framework of the Rice and Tracey Eq. [3] and similar to the CVGM. The effect of nonproportional loading in the stress space is incorporated by the quantity κ determined in Eq. (6b).

As described through Eqs. (6a)–(6e), the WM model has six cali-

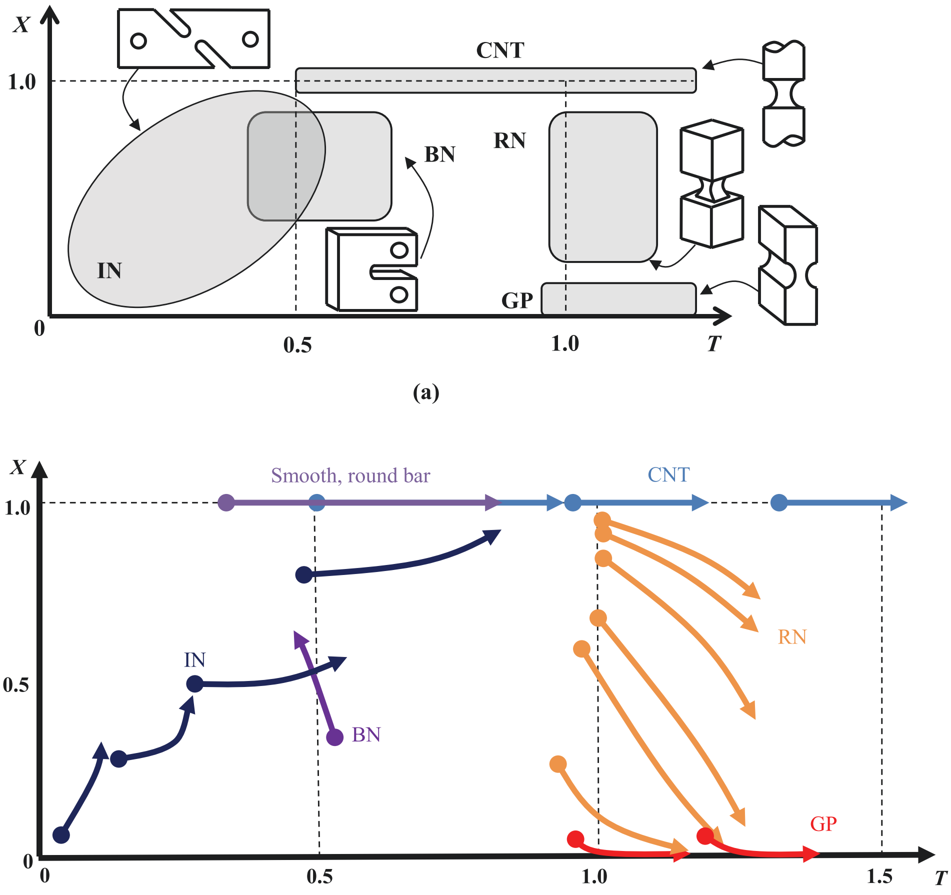

(a)

(b)

Fig. 3. Interrogation of stress trajectories at fracture locus in various specimens (a) regions of stress-space interrogated, and (b) evolution of triaxiality and Lode angle parameter over loading history.

bration parameters, $c_{14,WM}$, m_{WM}, $c_{3,WM}$, $c_{4,WM}$, $c_{5,WM}$, and $c_{6,WM}$, although Wen and Mahmoud [12] suggest that the last term $c_{6,WM}$ may be set to 0 for most metals. The validation basis for the WM model includes monotonic datasets on 2024-T351 Aluminum (Bao [18], and Seidt [19]), Al 5083 Aluminum Alloy (Gao et al., [20]), Weldox 420 and 960 steels (Barsoum and Faleskog [21]), A710 Steel (Wierzbicki et al. [22]), 1045 Steel (Bai et al. [23]; Bai [24]), and TRIP 780 steel (Dunand and Mohr [25]). These monotonic datasets feature experiments on hollow notched torsion specimens, grooved plate specimens, CNT specimens, butterfly specimens as well as flat specimens with a hole. The model was also validated against cyclic data sets on 1045 steel by Bai [26], on 2024-T351 Aluminum (Bao and Treitler [27]), and on A572 steel by Kanvinde and Deierlein [4,5]. The cyclic aspects of the model were validated only against CNT specimens (high-triaxiality, axisymmetric stress states), whereas the monotonic aspects were validated against a broader, albeit somewhat limited dataset. Specifically, the only low-triaxiality (i.e., $T < 0.5$) specimen i.e., the torsion test featured only one value of the Lode parameter (i.e., $X = 0$) corresponding to plane strain. The WM model assumes that the general trends noted in monotonic response and reflected in corresponding models (i.e, Wen and Mahmoud [28], Bao and Wierzbicki [29]) are also valid under cyclic/ULCF conditions.

Xiang et al. [30] proposed a criteria for aluminum, independently termed the Ultra-Low Cycle Fatigue model. Their model follows a similar general functional form to the VGM, but proposes a novel cyclic damage scheme. In the Xiang model, there is not restoration of damage on compressive cycles, and the cyclic fracture response is captured by varying damage rates during the isotropic and kinematic portions of the strain hardening response. The simplicity of this degradation model is attractive in comparison to models with many calibration parameters, but the separation of isotropic and kinematic hardening may not be straightforward in all cases [44]. Like the above models, the Xiang model is developed and calibrated for high-triaxiality specimens of constant X parameter, and may not be valid outside of that range.

Other notable models include Jia and Kuwamura [31], and Huang and Zhao [32] that consider only the effect of triaxiality, adaptations of Coffin-Manson type relationships (e.g., Kermajani et al. [33]; Xue [34]), or refinements to previously published models, such as the CVGM (e.g., Pereira et al. [35]). Another approach involves the use of fracture energy (e.g., see Martinez et al. [36]) to predict ULCF, albeit in a coupled sense, i.e., modifying the constitutive response of the material.

Despite the variety of models discussed above, a careful analysis shows close agreement (and low error) for axisymmetric, high triaxiality, and monotonic stress states. There is significantly less agreement in the models extended from that region – either in the variety of cyclic degradation rules, the treatment of low triaxiality levels, or the effect of the Lode angle parameter. This divergence is due to the scope, not the quality, of the models – as they are generally not focused on capturing the fracture process in these conditions.

3. The stress weighted ductile fracture model (SWDFM)

While significant progress has been made in developing ductile fracture criteria, knowledge gaps remain in development and validation of models over a broad stress space and inelastic loading history. Owing to the prevalence of CNT data, previous model developments have emphasized application to axisymmetric ($X = 0$) and high triaxiality ($T > 1$) stress conditions. As illustrated in the *T-X* specimen map of Fig. 3a, it is possible to interrogate a broad range of triaxiality, from $|T| \cong 0$ up to $|T| \cong 1.5$, and Lode parameters, from $X = 0$ up to $X = 1.0$, with the test specimen geometries shown in Fig. 2. The corresponding map of idealized *T-X* stress trajectories at the points of fracture initiation, shown in Fig. 3b, further illustrates how T and X typically vary during inelastic loading, from the onset of yielding (circle marker) to the initiation of fracture (arrow head marker). Note that the fracture initiation trajectories generally occur in the geometric center of the critical cross section of the fracture specimens.

With the goal to develop a model that can reliably capture ULCF ductile fracture over the entire range of stress states encountered in structures, a new model is proposed that incorporates insights from past studies and will be later shown to perform well against a large set of tests with variable stress–strain fields and loading conditions. Similar to previously developed models, the essence of the model is that fracture described as a functional form $f(\widetilde{\sigma}, \widetilde{\varepsilon})$ within the damage evolution Eq. (1). Development of the proposed functional form was guided by the following four goals:

1. When calibrated appropriately and implemented through accurate finite element simulations, the model should be able to predict experimental response (i.e., observed instants of fracture) and its dependence on stress and strain loading histories.
2. The functional form should minimize the number of free parameters that require calibration for each material, thereby facilitating its practical implementation while reducing the tendency for model overfitting (Webb [37]).
3. In cases where the experimental data is sparse (e.g., with respect to low-triaxiality situations), the functional form should reflect trends observed in computational cell simulations of void growth and shrinkage, which extend the theoretical void growth models.
4. The functional form should represent the fundamental processes of ULCF and ductile fracture as evidenced by fractographical studies, including microvoid growth and shrinkage/collapse as well as deterioration processes due to cyclic loading.

Goals 1 and 2 above are self-explanatory, whereas goals 3 and 4 require some additional discussion. Regarding goal 3, a comprehensive set of microvoid cell models were simulated as part of a related study (Cooke [38]) to understand better the microvoid growth/shrinkage under various stress states and loading histories. The microvoid simulations by Cooke loaded the void arrays in a controlled manner (e.g., a constant, predetermined stress state under a prescribed plastic strain history) for conditions that are otherwise challenging to control in laboratory specimens. The void simulations interrogated several parameters including: (1) void fraction and shape (2) a comprehensive range of stress states in the $T - X$ space, (3) monotonic tension and compression, as well as cyclic loading histories, (4) single as well as multivoid arrays, (5) presence of rigid inclusions within the voids, which interact with the shrinking/collapsing void under compression, and (6) constitutive response of the steel matrix material. Representative results, shown in Fig. 4, include the finite element mesh of a microvoid-array cell and evolution of microvoid size under monotonic and cyclic loadings. The main observations from these simulations, pertinent to this study are the following:

- Under monotonic loading (see Fig. 4b) with variation of triaxiality, the void growth rate $(1/R_0) \times (dR_0/d\varepsilon_p)$ closely follows the hyperbolic sine relationship with respect to triaxiality initially proposed by Rice and Tracey [3]. Notably, this figure shows the void growth rate approaches zero for $T = 0$, which is consistent with the hyperbolic sine form of Eq. (2) and is a feature that is lost in the simplified single exponential from of Eq. (3) (which is prevalent in the ductile fracture literature). Similar simulations with respect to the Lode parameter were inconclusive – no significant variation in the void growth simulations was observed. As the Lode parameter effect has been conclusively demonstrated experimentally, it appears likely that the effect exists but is difficult to simulate in microvoid models.
- Fig. 4c shows cyclic void evolution under a fixed magnitude of triaxiality, which changes sign as the loading reverses. Note that the initiating inclusion is not modeled, permitting the void to shrink below the original size. Even so, the void growth rate is consistently larger under positive triaxiality as compared to negative triaxiality. This suggests a net accumulation of void growth, that may be

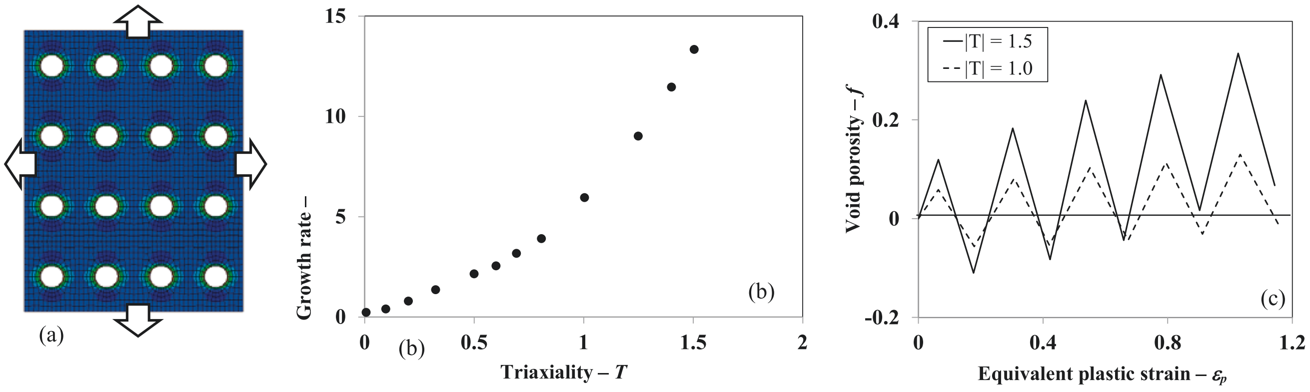

Fig. 4. Microvoid Cell Simulations: (a) Continuum model of void array, (b) monotonic void growth rates as a function of triaxiality, (c) cyclic porosity evolution (Cooke [36]).

interpreted as irrecoverable damage biased in the direction of positive triaxiality.

- Void growth rates decrease as the Lode parameter X varies from 1 to 0 (i.e., axisymmetric to plane strain conditions). This trend is in agreement with monotonic test data from (Bao [18]) for tests on 2024-T351 Aluminum, however, it contradicts observations from experiments presented later in this study in which fracture is observed to occur at lower plastic strains in specimens with axisymmetric stress states relative to those in plane strain.

Related to goal 4, fractographic observations conducted as part of this study and previous studies (Kanvinde and Deierlein [9]) qualitatively corroborate observations of the microvoid simulations and ULCF testing. Shown in Fig. 5 are fracture surfaces from RN specimens with similar values of T but different Lode parameters ($X = 0.9$ and 0.1). While the dimpled fracture surfaces provide clear evidence of the void growth fracture mechanism, comparisons between the dimple sizes shapes for these and other images are inconclusive with regard to the influence of the Lode parameter on microvoid shape or size. In previous studies, Kanvinde and Deierlein [5] have noted that the dimple sizes are indicative of the characteristic length parameter (l^*), which is important for situations with high stress–strain gradients, and that fractures associated with ULCF loading tend to have shallower dimples with lower critical void growth limits as compared to monotonic loading.

3.1. Development of functional form

Following the considerations outlined above, the functional form for the damage rate, i.e., $f(\widetilde{\sigma}, \widetilde{\varepsilon})$ was constructed to include dependencies on triaxiality T, the Lode parameter X , as well as irrecoverable damage caused by cyclic loading. Two strategies used in the development are:

- The functional form is expressed as a product of two terms, i.e., $f(\widetilde{\sigma}, \widetilde{\varepsilon}) = g(T) \times h(X)$, to decompose and isolate the effects of T and X , which allows their independent development based on trends in test data and the microvoid simulations.
- Relying on microvoid simulations that reflect unequal growth rates under positive and negative triaxiality, the effect of cyclic deterioration is handled within the void growth/shrinkage subfunction, $g(T)$. This is a departure from the strategy followed in prior work by the authors (Smith et al. [39]; Kanvinde and Deierlein [40]), where as shown in Eq. (4), the cyclic damage was represented by a separate exponential decay term. Aside from aligning better with the microvoid simulations, this change simplifies the functional form and eliminates a material calibration parameter.

The following subfunction $g(T)$ is developed to characterize the dependence of damage on triaxiality:

$$g(T) = C_{SWDFM} \times \left[exp(\gamma_{SWDFM} T) - \left(\frac{1}{\beta_{SWDFM}} \right) exp(-\gamma_{SWDFM} T) \right] \tag{7}$$

The function is similar to the analytical Rice and Tracey [3] equation, and to the monotonic triaxiality-based criteria presented earlier by the authors (14B])with two key differences. First, the term β_{SWDFM} establishes a difference between void growth and shrinkage rates (governed by the two exponential terms respectively). Values of β_{SWDFM} greater than unity bias the damage rate towards positive triaxiality, the function thus captures the irrecoverable damage under cyclic loading. β_{SWDFM} is attached to the second exponential term in the equation (which is small for high, positive triaxiality) in order that C_{SWDFM} may be

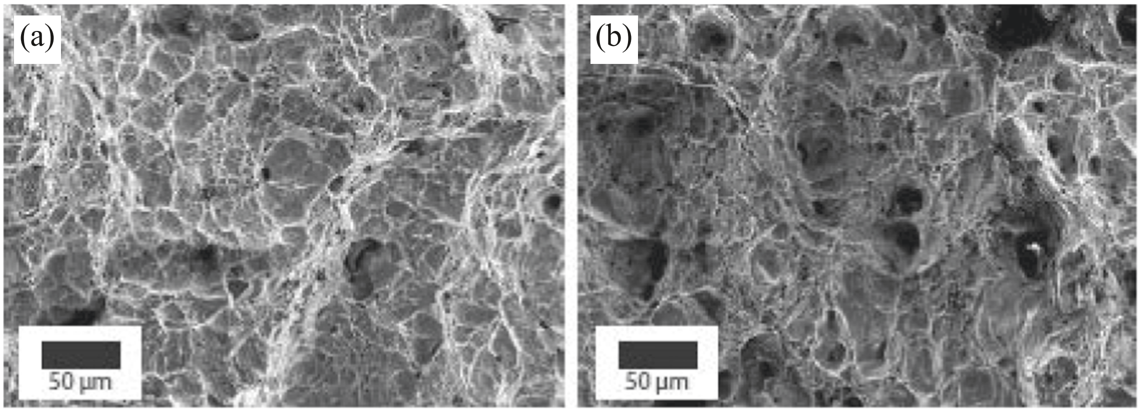

Fig. 5. Fractographs from two IN specimens: (a) T = 1.3, X = 0.9, and (b) T = 1.1, X = 0.1.

approximatly calibrated through the use of monotonic specimens alone. Second, as determined by Smith et al. [15], the term γ_{SWDFM} is set to a fixed value of 1.3, in contrast to the value of 1.5 derived analytically by Rice and Tracey [3,40]. This deviation is attributed to the hardening properties of the metal matrix, the void coalescence process, and other factors not present in the idealized derivation by Rice and Tracey [3]. The term C_{SWDFM} is a calibrated material parameter inversely related to deformation capacity.

The second subfunction, $h(X)$, is developed to characterize dependence on the Lode parameter:

$$h(X) = exp[k_{SWDFM}(|X| - 1)] \tag{8}$$

The function constructed to have a value of unity at $X = 1$ (i.e., axisymmetric loading), thus facilitating calibration of the C_{SWDFM} parameter (from Eq. (10)) directly from CNT tests that have the axisymmetric stress state. The parameter k_{SWDFM} controls the dependence of damage on the Lode parameter and may take any positive or negative value. A positive value of k_{SWDFM} results in lower damage accumulation in the plane strain ($X = 0$) state, relative to the axisymmetric loading, which is consistent with the experimental observations of this study.

Combining the two subfunctions, the SWDFM can be expressed as:

$$D = \int dD = C_{SWDFM} \times \int_0^{\varepsilon_p} \left[exp(1.3T) - \left(\frac{1}{\beta_{SWDFM}}\right)exp(-1.3T)\right] \cdot exp[k_{SWDFM}(|X| - 1)] \cdot d\varepsilon_p \geq 1 \tag{9}$$

where the free material dependent parameters are C_{SWDFM} and k_{SWDFM} and β_{SWDFM}, which can be determined by calibration to test data.

4. Experiments and complementary continuum finite element simulations

A series of 66 experiments were conducted to examine ULCF under various stress states and loading histories. As summarized in Table 1 and illustrated in Fig. 2, these tests included five different types of specimens and two structural steels, i.e., A572 Grade 50 (nominal yield 345 MPa) and A36 (nominal yield 250 MPa) steels. Key characteristics of the specimens are described below, with more details of their development and testing provided by Smith et al. [39] and Terashima et al. [41]:

Circumferentially Notched Tensile (CNT) Specimens (Fig. 2a): As noted previously and illustrated in Fig. 3, CNT specimens produce (1) an axisymmetric stress state (i.e., $X = 1$) at the center of the specimen where ductile fracture typically initiates and (2) moderate to high triaxiality under remote tension and compression loading (i.e., $1 < |T| < 1.6$). The triaxiality can be controlled conveniently through the notch radius R_N and root diameter D_{UN}. CNT tests are popular because they are relatively easy to fabricate and test, and they provide reliable and consistent results.

Rectangular Notched (RN) Specimens (Fig. 2b): As shown in Fig. 3, the RN specimens allow the independent interrogation of triaxiality (in the range $1.0 \leqslant |T| \leqslant 1.5$) through adjustment of notch radius (in a manner similar to the CNT specimens) as well as the Lode parameter ($0.3 \leqslant X \leqslant 1.0$) through adjustment of the aspect ratio of the notched cross section. Specifically, a square cross section ($t_{NR}^{I}/t_{NR}^{II} = 1$) results in an axisymmetric stress state at the center of the notched region where fracture initiates, whereas an infinitely long cross section ($t_{NR}^{I}/t_{NR}^{II} = \infty$) results in a plane strain condition.

Grooved Plate (GP) Specimens (Fig. 2c): With elongated cross section geometries where $t_{NR}^{I}/t_{NR}^{II} \geqslant 6$ the GP specimens essentially achieve plane strain conditions ($X = 0$) at the midpoint of the notched region where fracture initiates. Similar to the RN specimens, the triaxiality in these may be varied in the range $0.9 < |T| < 1.5$ by adjusting the notch radius R_N. As illustrated in Fig. 3a, comparative tests of GP and CNT specimens provide an effective way to isolate the effect of Lode parameter on fracture.

Inclined Notch (IN) Specimens (Fig. 2d): The IN specimens are similar to butterfly shaped specimens that have been used in other studies, where the stress state at the critical section can be modified by varying the notch radius and the orientation (relative to the loading axis). As illustrated in Fig. 3a, the IN specimens allow for interrogation of fracture under low triaxialities ($0.1 \leqslant |T| \leqslant 0.7$) and a wide range of Lode parameters (in the range $0.15 \leqslant X \leqslant 0.8$).

Blunt Notched (BN) Specimens (Fig. 2d): The BN specimens are intended to more closely mimic inelastic cyclic loading conditions in structural members without a prescribed notch region. In contrast to other specimens, the internal stress state is less contrived and is affected more by inelastic distortion of the specimen. Typical stress states at fracture initiation are in the range of $T = 0.4$ to 0.6 and $X = 0.4$ to 0.8.

The specimens were loaded in a uniaxial 100 kN capacity hydraulic testing machine under monotonic or reversed cyclic loading as per the protocols referenced in Table 1. The applied load and gage length displacement (see Fig. 2) were monitored and the instant of ductile rupture was identified either through (1) a sudden change in slope of the load–displacement response, for the CNT, RN, and GP specimens, or (2) through visual observations made with a magnifying lens, for the BN and IN specimens, where the initiation of fracture is not apparent in the load–displacement curve. Examples of the load–displacement response from the CNT, RN and GP specimens are shown in Fig. 6, where the change in response due to fracture is clearly evident. Also shown in the figure are results of computational finite element simulations, which are described next.

Continuum finite element simulations were conducted for each set of the tests to determine the local stress and strain histories for input to the ductile fracture models. Shown in Fig. 7a-c are the finite element models for three of the specimen geometries, which are generally representative of models for other specimens. The finite element models were based on the measured as-machined specimen geometry. The models utilized planar symmetry or axisymmetry for computational efficiencies, and the meshes were refined in the regions of high gradients to ensure convergence. The models were developed and run using ABAQUS [42], where the CNT specimens were modeled with axisymmetric 8-node quadrilateral elements and the other specimens were modeled with 3-dimensional 20-node brick elements – all with reduced integration. The simulations modeled large displacements and strains, where the steel constitutive response was represented through von Mises plasticity with isotropic and kinematic hardening, defined by a two-backstress variant of the Armstrong-Frederick [43] model. The constitutive models parameters were calibrated using an automated process, based on the Particle Swarm Optimization approach [44], to minimize the error in the load-deformation curves across all specimens and loading regimes.

The stress and strain histories recorded in the finite element simulations are processed through the SWDFM to determine the location of fracture initiation. As shown by the white circle markers in Fig. 7a-c, the point of simulated fracture initiation is at the center of the notched sections in the CNT, GP and IN specimens, which is consistent with the fracture locations observed in the tests. The stress and strain histories recovered at these locations (along with corresponding locations from

Table 1
Summary of test specimens.

Steel Grade	Specimen	Critical dimensions	Loading	Replicates	T_{avg} [1]	X_{avg}
ASTM A572 − 345 MPa	CNT	$D_{UN} = 12.7$ mm, $D_{NR} = 5.36$ mm, $R_N = 7.27$ mm	Monotonic	2	1.6	1
		$D_{UN} = 12.7$ mm, $D_{NR} = 5.21$ mm, $R_N = 1.45$ mm	Cyclic (CTF)[2]	1	1.6	1
	GP	$t_{UN} = 11.9$–12.7 mm, $t_{NR} = 2.26$–2.59 mm, $R_N = 1.2$–3.2 mm, $W_N = 25.4$ mm	Monotonic	3	0.9–1.25[3]	0
	RN	$t^I_{UN} = t^{II}_{UN} = 25.4$ mm, $t^I_{NR} = 7.75$–11.15 mm, $t^{II}_{NR} = 5.13$–7.58 mm, $R_N = 3.18$ mm	Monotonic	6	1.2–1.5[3]	0.3–1.0[3]
	IN	$\theta = 30°$, $R_N = 3.18$ mm, $t_{NR} = 4.42$ mm	Monotonic	1	0.7	0.8
		$\theta = 30°$, $R_N = 1.59$ mm, $t_{NR} = 4.72$ mm	Monotonic	1	0.65	0.7
		$\theta = 30°$, $R_N = 3.18$ mm, $t_{NR} = 5.08$ mm	Cyclic (C-PTF)[3]	1	0.6	0.8
		$\theta = 30°$, $R_N = 1.59$ mm, $t_{NR} = 5.84$ mm	Cyclic (CTF)	1	0.45	0.4
		$\theta = 50°$, $R_N = 3.18$ mm, $t_{NR} = 5.08$ mm	Monotonic	1	0.45	0.55
		$\theta = 50°$, $R_N = 3.18$ mm, $t_{NR} = 4.28$ mm	Monotonic	1	0.45	0.6
		$\theta = 50°$, $R_N = 3.18$ mm, $t_{NR} = 4.83$ mm	Cyclic (C-PTF)	1	0.4	0.5
		$\theta = 70°$, $R_N = 3.18$ mm, $t_{NR} = 4.61$ mm	Monotonic	1	0.25	0.4
		$\theta = 70°$, $R_N = 3.18$ mm, $t_{NR} = 5.08$ mm	Cyclic (CTF)	1	0.2	0.3
		$\theta = 70°$, $R_N = 3.18$ mm, $t_{NR} = 4.83$ mm	Cyclic (C-PTF)	1	0.2	0.3
		$\theta = 90°$, $R_N = 3.18$ mm, $t_{NR} = 4.51$ mm	Monotonic	1	0.1	0.15
		$\theta = 90°$, $R_N = 3.18$ mm, $t_{NR} = 4.95$ mm	Cyclic (C-PTF)	1	0.1	0.15
ASTM A36 − 250 MPa	CNT	$D_{UN} = 12.7$ mm, $D_{NR} = 6.35$ mm, $R_N = 12.7$ mm	Monotonic	1	0.5	1
			Cyclic (CTF)	6		
		$D_{UN} = 12.7$ mm, $D_{NR} = 6.35$ mm, $R_N = 3.18$ mm	Monotonic	1	1	
			Cyclic (CTF)	6		
		$D_{UN} = 12.7$ mm, $D_{NR} = 6.35$ mm, $R_N = 1.27$ mm	Monotonic	1	1.5	
			Cyclic (CTF)	6		
	GP	$t_{UN} = 9.53$ mm, $t_{NR} = 2.54$ mm, $W_N = 19.05$ mm, $R_N = 2.03$ mm	Monotonic	3	1	0
		$t_{UN} = 9.53$ mm, $t_{NR} = 2.54$ mm, $W_N = 19.05$ mm, $R_N = 0.76$ mm		3	1.5	0
	RN	$t^I_{UN} = t^{II}_{UN} = 19.05$ mm, $t^I_{NR} = 8.89$ mm, $t^{II}_{NR} = 5.08$ mm, $R_N = 5.08$ mm	Monotonic	3	1	0.6
		$t^I_{UN} = t^{II}_{UN} = 19.05$ mm, $t_{NR,1} = 9.53$ mm, $t_{NR,2} = 7.11$ mm, $R_N = 1.52$ mm		3	1.5	0.8
	BN	$L_{PN} = 25.4$ mm, $B = 19.05$ mm, $R_N = 2.03$ mm, $L_P = 15.24$ mm, $L_V = 68.56$ mm	Monotonic	3	0.5	0.5
			Cyclic (CTF)	6		

[1] Values shown are average values of triaxiality magnitude and Lode parameter over the loading history.

[2,3] CTF represents constant amplitude cyclic loading (Cycle-To-Failure), whereas C-PTF represents cyclic loading followed by a tensile excursion (Cycle and Pull To Failure). Details of loading histories are available in Smith et al., [39] and Terashima [41].

[4] The GP and RN series represent a range of geometry which are spaced within these bounds, and summarized for brevity. A complete test summary is available in Smith et al. [39].

other specimens) are subsequently processed through all four fracture models (CVGM, KK, WM and SWDFM) to examine and compare their effectiveness in predicting fracture.

5. Results and discussion

The four fracture models are evaluated using data from the 66 tests summarized in Table 1, which include two structural steels and reflect a wide range of stress triaxiality, Lode parameter and loading history. The values of characteristic X and T in Table 1 are determined, as outlined in more detail later, from the finite element simulations. For an objective comparative assessment of the four fracture models, three free parameters of each are first calibrated against the test data using the following process:

1. The free material parameters for each of the criteria are identified, as listed in Table 2. For the CVGM and WM models, the free parameters are as published in the corresponding original references, whereas for the KK model, in addition to $d_{cr,KK}$, which is identified as the sole free parameter in the original publication, $a_{1,KK}$, $b_{1,KK}$, $a_{2,KK}$, and $b_{2,KK}$ are also considered free parameters in this study. This is because trial studies showed the single parameter to be insufficient to predict fracture in a satisfactory manner. Assuming all parameters to be free significantly improves model performance.
2. A full-factorial sampling grid of trial parameter sets is generated, where each free parameter (for each model) is varied within a wide

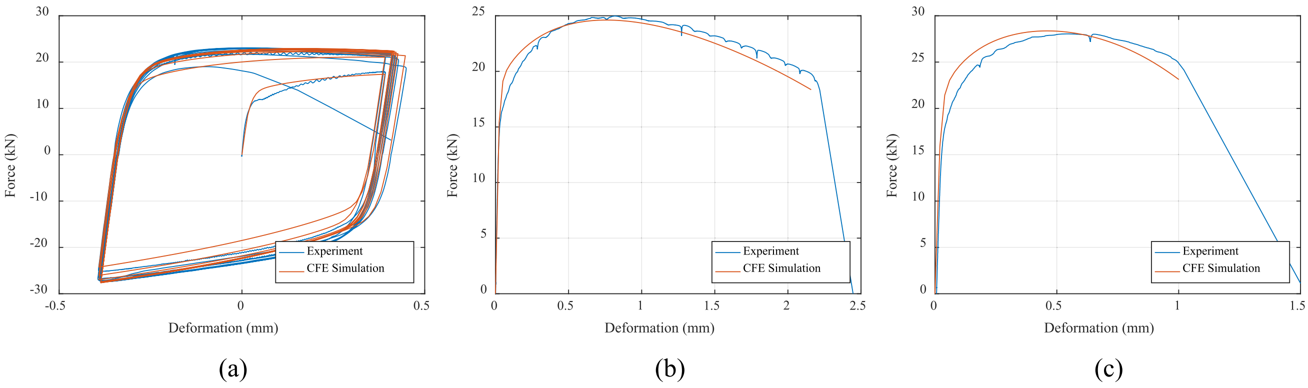

(a) (b) (c)

Fig. 6. Force-deformation curves of experimental and continuum finite element simulations of: (a) CNT specimen, (b) RN specimen and (c) GP specimen.

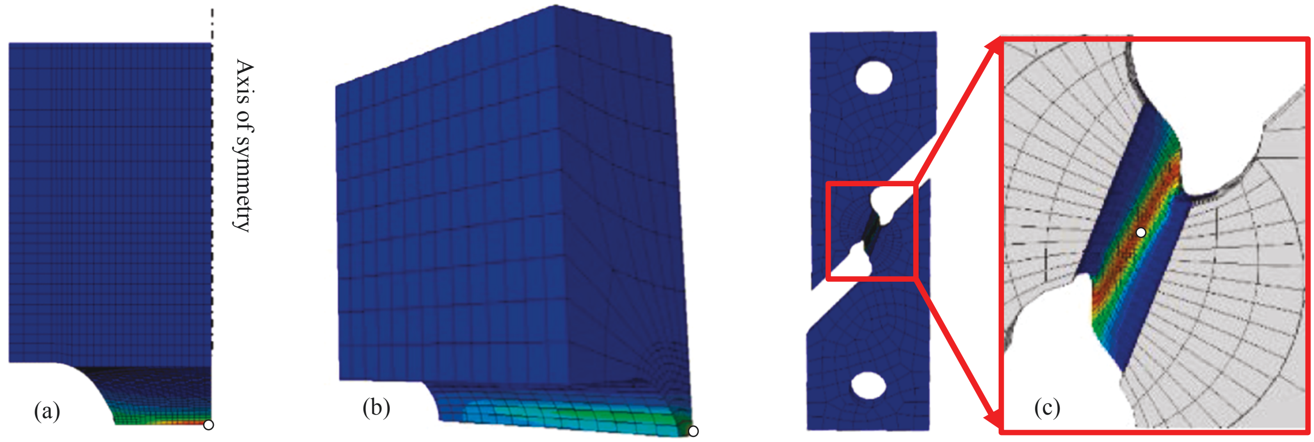

Fig. 7. Continuum Finite Element simulations showing contours of D_{SWDFM} for: (a) axisymmetric model of CNT specimen, (b) one-eighth symmetric model for GP specimen, and (c) three-dimensional model for IN specimen; white circle represents location of predicted fracture.

Table 2
Calibrated model parameters and least squared error.

Model	Optimal Parameter values					$\in = (1/n) \times \sum_{i=1}^{n} \left\| 1 - D_j^{fracture,i} \right\|$	$\in_{balanced}$
SWDFM	C_{SWDFM}	k_{SWDFM}	β_{SWDFM}				
A572	0.62	0.5	2.0			0.135	0.113
A36	0.24	0.45	2.0			0.153	0.143
CVGM	η_{CVGM}	λ_{CVGM}					
A572	0.4	0.35				0.182	0.219
A36	0.15	0.67				0.320	0.277
KK	$a_{1,KK}$	$b_{1,KK}$	$a_{2,KK}$	$b_{2,KK}$	$d_{cr,KK}$		
A572	2.08	0.7	1.0	0.5	1.19	0.229	0.269
A36	1.04	0.5	1.0	1.9	1.33	0.172	0.212
WM	$c_{3,WM}$	$c_{4,WM}$	$c_{5,WM}$	$c_{14,WM}$	m_{WM}		
A572	2.7	−1.40	3.25	5.0	1.0	0.148	0.122
A36	6.7	−1.35	2.5	8.0	1.1	0.175	0.181

range. Then, for each of these trial parameter sets, a realization of the damage evolution is determined using the stress and strain histories from the finite element analyses at the fracture location for each of the 66 tests. For example, for the SWDFM model, the damage evolution for a particular test is determined as:

$$D_j^{fracture,i} = C_{SWDFM,j} \int_0^{\varepsilon_p^{fracture,i}} [exp(1.3T) - exp(-1.3T)] \cdot \left(\frac{1}{\beta_{SWDFM}}\right) exp\left[k_{SWDFM,j}(|X| - 1)\right] \cdot d\varepsilon_p \tag{10}$$

where $D_j^{fracture,i}$ denotes the damage estimated by integrating the SWDFM to the experimentally observed location and instant of fracture in the experiment i for the trial parameter set j comprising $C_{SWDFM,j}$, and $k_{SWDFM,j}$. An ideal prediction of fracture would result in $D_j^{fracture,i} = 1$. Thus, the optimal parameter set j for a particular material is determined as the one that minimizes the average squared error $\in = (1/n) \times \sum_{i=1}^{n} \left(1 - D_j^{fracture,i}\right)^2$ over all n tests on that material. Similar calibrations are conducted for all four fracture models. Note that these computations are relatively quick to perform, since they only entail repeated post-processing of stress and strain data for a single location from finite element simulations of the 28 individual specimen and loading configurations in Table 1. Therefore, once the models and optimization workflow is set up, it is relatively easy to interrogate multiple trial parameter sets for each fracture model.

The optimal parameter sets for each of fracture model and steel (along with the corresponding average errors) are summarized in Table 2. For the SWDFM specifically, β_{SWDFM} was found to be 2.0 for both materials, with the calibration relatively insensitive to small adjustments. The parameter κ_{SWDFM} is also noted to be similar for both tested materials. One or both of these parameters may be material-independent. Additionally, the above calibration process is appropriate for validation and comparison of criteria, but could potentially induce biases for model development in an unbalanced data set (e.g. significantly more CNT specimens than GP specimens). Regarding the SWDFM, the constituent parts of the model were individually developed in prior studies: *f(T)* through a broad study of axisymmetric specimens [15] and *g(X)* through study of the individual RN data set [39].

To interrogate the effects of any potential bias resulting from the uneven number of specimen types in each data set, a second error measure was also calculated, $\in_{balanced}$. In the calculation of this error measure, the number of tests of each specimen type was set to be equal. This was done by counting each test multiple times for the specimen types which were under-represented in the original dataset. For example, the A572 data set contains 3 CNT specimens, 3 GP specimens, 12 IN specimens and 6 RN specimens. To balance the data set, each CNT and GP test was replicated four times, while each RN test was replicated twice. The resulting balanced data set thus contains 48 data points, consisting of 12 tests of each specimen type. The average error for this new, hypothetical data set was then calculated as described previously. A significant difference between the two error measures might indicate a bias in the calibration results due to the unbalanced number of tests for each specimen type. As can be seen in Table 2, the average error and the balanced error for both datasets for the SWDFM are very similar, indicating that minimal bias occurs due to the nature of the datasets.

Referring to Table 2, the average errors indicate the overall fit of the

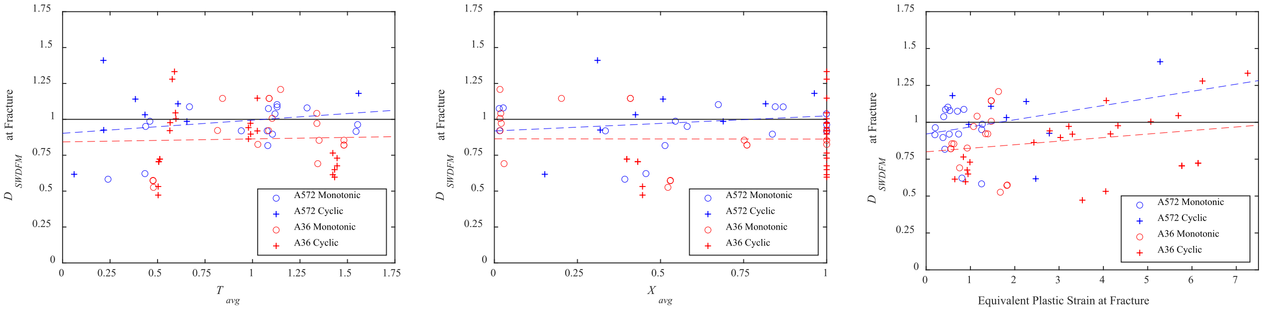

Fig. 8a. Damage at fracture using optimal parameters plotted against average triaxiality, average Lode angle parameter, and equivalent plastic strain for SWDFM.

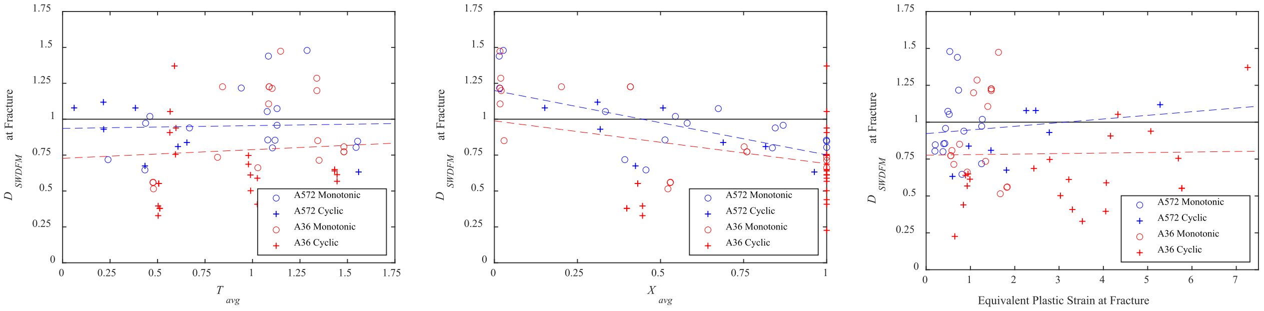

Fig. 8b. Damage at fracture using optimal parameters plotted against average triaxiality, average Lode angle parameter, and equivalent plastic strain for CVGM.

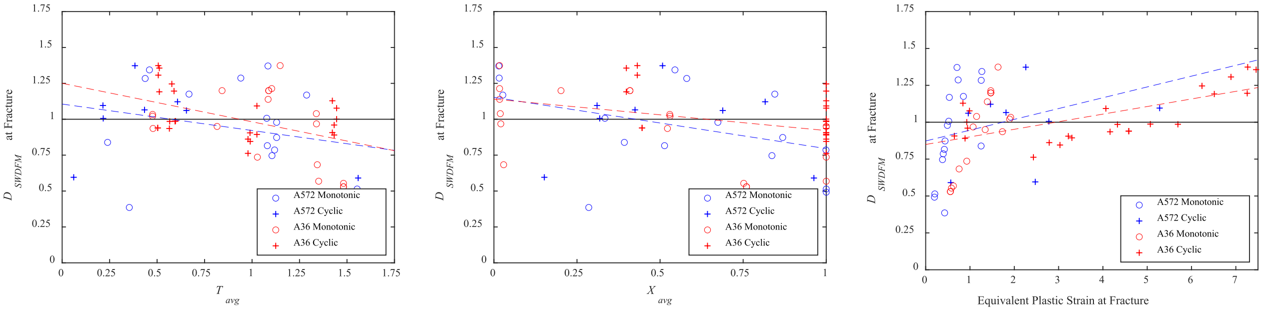

Fig. 8c. Damage at fracture using optimal parameters plotted against average triaxiality, average Lode angle parameter, and equivalent plastic strain for KK.

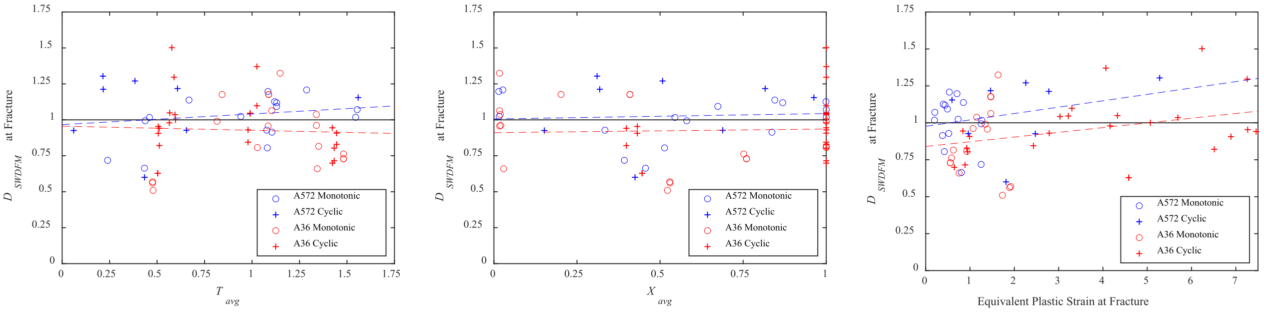

Fig. 8d. Damage at fracture using optimal parameters plotted against average triaxiality, average Lode angle parameter, and equivalent plastic strain for WM.

model, they do not help to discern trends with respect to the influential loading variables. To examine such trends, the calculated damage parameters $D_{optimal}^{fracture.i}$(i.e., the damage computed for the observed fracture point in each test using the optimal set of parameters shown in Table 2) are plotted versus triaxiality, T, Lode parameter, X, and the equivalent critical plastic strain, $\varepsilon_p^{fracture}$, in Figs. 8a-d. As illustrated previously in Fig. 3b, the values of T and X vary over the loading history from the onset of yielding up to fracture. For the purposes of the trend comparisons in Figs. 8a-d, the values of T_{avg} and X_{avg} are averaged over the loading history to provide a representative value for each test, using the following equations:

$$T_{avg} = \left(1/\varepsilon_p^{fracture}\right)\int_0^{\varepsilon_p^{fracture}} T\cdot d\varepsilon_p \tag{11}$$

$$X_{avg} = \left(1/\varepsilon_p^{fracture}\right)\int_0^{\varepsilon_p^{fracture}} X \cdot d\varepsilon_p \qquad (12)$$

Plots for the three parameters (T_{avg}, X_{avg}, $\varepsilon_p{}^{fracture}$) are shown in Figs. 8a-d for each of the four models. The markers in the plots distinguish between the two steels, as well as monotonic versus cyclic tests. In addition, linear trendlines are provided for each dataset on each plot. The following are some key observations from these comparisons:

1. As summarized in Table 2, the fracture models provide average errors ranging from 0.135 (for the A572 Steel for SWDFM), to 0.32 (for the A36 Steel for CVGM). The SWDFM and WM models that explicitly include a dependence on the Lode parameter show significantly better performance as compared to the CVGM and KK that do not have a Lode parameter term and were developed primarily based on data from axisymmetric CNT test specimens. Notably, the SWDFM has the lowest error despite having only three free material parameters.
2. Referring to Fig. 8a, the SWDFM does not appear to show a bias or a significant variation in accuracy with respect to any of the loading parameters, T_{avg} or X_{avg}, or $\varepsilon_p{}^{fracture}$. Combined with the fact that this model has a minimal number of free calibration parameters, this observation suggests that the SWDFM successfully represents the key physical processes for ULCF fracture. Regarding the number of free parameters, the CVGM has two parameters but does not consider the dependence of fracture on X. As the X dependence appears to be material-dependent, the SWDFM and CVGM are equally efficient. Referring to the scatter of points within the plots, it is apparent that the SWDFM does not show a bias with respect to either the steel material or type loading (monotonic vs cyclic).
3. Referring to Fig. 8b, the CVGM results show clear variation with respect to $\varepsilon_p{}^{fracture}$ and X_{avg}, while the results are not sensitive to T_{avg}. The CVGM is particularly inaccurate for the A36 steel, as well as for tests with large $\varepsilon_p{}^{fracture}$, which are indicative of tests with a large number of cycles. This is not surprising, given that the CVGM was developed primarily based on CNT specimens that have moderate-high triaxiality and were loaded with fewer cycles, compared to those applied in the validation data set.
4. Referring to Fig. 8c, the trends for the KK model are similar to those of the CVGM, both qualitatively and quantitatively. It should be noted that the results shown in Table 2 and Fig. 8c are based on calibration of five free material parameters. Had the original KK model formulation been applied, which only varied the single material parameter $d_{cr,KK}$, the errors and bias trends would be much larger.
5. Referring to Fig. 8d, results for the WM model are similar to those of the SWDFM model, where there is no significant trend with respect to T_{avg} or X_{avg}, or $\varepsilon_p{}^{fracture}$. However, as shown previously in Table 2, the errors for the WM are slightly larger than for the SWDFM, in spite of the fact that the WM model requires five parameters to calibrate, versus three for the SWDFM.

Another metric to consider for model validation relates to the potential of model overfitting, wherein the model results display low error when applied retrospectively to the test data that they were calibrated to, but exhibit larger errors when applied in a predictive sense. This phenomenon is attributable to models that are overly complex and do not accurately represent the underlying relationships between the variables. Models with a large number of fitting parameters are particularly susceptible to overfitting. To evaluate for this, Leave-One-Out-Cross-Validation, Webb [37]) is conducted for each of the models. Specifically, for each model and steel material, the optimal set of parameters is first determined as per the procedure outlined above, i.e., by minimizing the squared damage error over the experiments with that material. However, unlike the calibration discussed above, the optimal parameters are determined by conducting the minimization over $n-1$ experiments, leaving one out. The fracture model with these calibrated parameters is then used to predict fracture in the remaining test, i.e., the one not used within the calibration set. Thus for each test i, the damage $D_{i\not\subset n}^{fracture,i}$ is determined. The subscript $i \not\subset n$ indicates that the damage is determined from a parameter set calibrated from all tests excluding test i. This process was repeated for all the tests, resulting in an averaged error estimate$\in_{LOOCV} = \frac{1}{n} \times \sum_{i=1}^{n}\left|1 - D_{i\not\subset n}^{fracture,i}\right|$, which is an indicator of the predictive ability of the fracture model. Table 3 summarizes the $\in_{LOOCV}$ values for each of the rupture criteria, and for each of the steels. Referring to the Table (the columns titled "$\in_{LOOCV}$)," the results reinforce the previous observations from Table 2 and Figs. 8a-d. Specifically, the CVGM and KK models show relatively high LOOCV errors as compared to the SWDFM with the lowest errors, closely followed by the WM. The differences are particularly apparent in the error data for cases where the models were calibrated with only the CNT and GP test data, and then used to evaluate all of the tests. These observations further suggest that both the SWDFM and WM capture better the inherent mechanisms controlling the ULCF fracture. Further, despite the larger number of calibration parameters of the WM model, it does not seem susceptible to overfitting, given its low LOOCV error. A closer inspection of Table 2 reveals why this may be the case. Specifically, referring to the optimally calibrated parameters for the WM model, the m_{WM}, $c_{4,WM}$, and $c_{5,WM}$ parameters are fairly close in value, possibly suggesting that they may not be material dependent for the structural steels studied herein. In fact, the remaining two parameters ($c_{3,WM}$ and $c_{14,WM}$) appear to characterize fairly well the material dependence of ULCF fracture.

Table 3
Results of validation studies.

	A572 – 345 MPa (Smith, 2014)			**A36 – 250 MPa (Terashima, 2018)**	
Method	$\in_{LOOCV}$	$\in$(calibrated with GP/CNT only)	$\in_{IN}$(calibrated with GP/CNT only)	$\in_{LOOCV}$	$\in$(calibrated with GP/CNT only)
CVGM	0.22	0.36	0.48	0.34	0.32
KK	0.22	0.40	0.61	0.18	0.17
WM	0.19	0.16	0.21	0.20	0.17
SWDM	0.15	0.14	0.18	0.16	0.17

Table 3 also includes error estimates when the four models are calibrated (as per the methodology outlined above) using only a subset of the data. The calibration set includes only the CNT and GP specimens; these are selected because they are relatively inexpensive to fabricate, instrument, and test, without the requirement for special fixtures. Specifically, the GP specimens may be conveniently tested using flat grips and an extensometer, whereas the CNT specimens may be tested using conventional grips for round bars, and an extensometer. The parameters calibrated in this manner are used to predict fracture in two sets of data for the A572 steel - one includes all the specimens, whereas the other includes only the IN specimens. For the A36 steel, IN specimens were not tested, so the prediction error is determined for the entire data set. For each prediction set, the average error is determined in a manner similar to that noted above for the LOOCV analysis. Referring to Table 3, for all models, the LOOCV error (which uses parameters calibrated from all types of specimens) tends to be lower than the prediction error resulting from the GP/CNT calibrations. However, for both the SWDFM and the WM models (which include Lode parameter dependence), the prediction errors are not significantly higher than the LOOCV. For example, when the SWDFM is calibrated only using the CNT and GP specimens, the prediction error for the A572 steel is 0.14 for the entire set, and 0.18 for the IN-only set; which is comparable to the LOOCV error 0.15. A similar outcome is noted for the A36 steel (0.16 LOOCV error, versus 0.17 CNT/GP error). This indicates that CNT and GP specimens can successfully characterize the key dependencies of fracture on T and X respectively, suggesting that a full interrogation of the *T-X* space (using more expensive IN specimens) may not be necessary for model calibration.

6. Summary and conclusions

The aim of this paper is to develop a criterion to characterize Ultra Low Cycle Fatigue fracture in structural steels over the wide range of stress states commonly encountered in structural details. To support the model development and calibration, 66 coupon scale experiments were conducted using two common steels, including specimens that interrogated a stress triaxiality ranging from 0.1 to 1.6 and Lode parameters from 0 to 1.0 under monotonic and cyclic loading histories. The model development was further informed by prior theoretical studies of void growth, microvoid cell simulations, and fractographic imaging to characterize the ductile fracture mechanism of void growth and coalescence. The proposed Stress Weighted Ductile Fracture Model (SWDFM) includes a dependence on stress triaxiality that was previously demonstrated by Smith et al. [15], modified by the unequal weighting of the positive (tension) and negative (compression) triaxiality terms to reflect irrecoverable damage under cyclic loading. The fracture model requires only three free parameters that can be independently calibrated from material tests.

The proposed SWDFM criterion was assessed against the experimental data, along with three other recently proposed ULCF rupture models (CVGM, KK, and WM). Of these, two (CVGM and KK) were developed primarily using high-triaxiality axisymmetric specimens for validation. As a result, these are unable to accurately characterize ULCF across the entire range of stress states. On the other hand, the SWDFM criterion is most successful, closely followed by the WM – both of these are based on specimens that interrogate a large range of triaxiality and Lode parameter. A cross-validation analysis confirms that the SWDFM is able to characterize ULCF with a fairly low error compared to the other criteria.

While this is encouraging, some limitations of the proposed SWDFM and other fracture models are important to note. First, the model has only been evaluated for two fairly similar low-carbon structural steels = . As the fundamental mechanism of void growth and coalescence is known to cause fracture in a wider range of materials, it is expected that this model, like other void-growth-based models, would be applicable to these materials. Expanded application of this criteria may demonstrate the parameters κ_{SWDFM} or β_{SWDFM} may be material independent, causing the model to be significantly easier to calibrate and apply. Other considerations not addressed in this paper, but important to its application, include: (1) evaluation of the characteristic length, which becomes necessary to apply the model to sharp stress–strain gradients, (2) spatial randomness in material properties, which is needed to scale the model to structural-scale applications (Pericoli and Kanvinde [45]). Finally, the ductile fracture criterion is only one part of the fracture assessment framework for steel structures. Reliable calculation of the internal stress and strain fields requires detailed finite element simulations with accurate constitutive models [44]. Moreover, the SWDFM fracture criterion is limited to evaluating fracture initiation, which is the precursor to crack propagation.

CRediT authorship contribution statement

Christopher Smith: Conceptualization, Methodology, Validation, Writing - review & editing. **Andy Ziccarelli:** Methodology, Validation, Formal analysis, Investigation. **Masao Terashima:** Methodology, Validation, Formal analysis, Investigation. **Amit Kanvinde:** Conceptualization, Methodology, Validation, Writing - review & editing, Supervision. **Gregory Deierlein:** Conceptualization, Methodology, Validation, Writing - review & editing, Supervision.

Declaration of Competing Interest

The authors declare that they have no known competing financial interests or personal relationships that could have appeared to influence the work reported in this paper.

Acknowledgments

This research was supported by the National Science Foundation under Grant Numbers CMMI-0825339, 1635043, 0825155, and 1634291. The contributions of Ryan Cooke (of Schuff Steel) to the microvoid simulations are gratefully acknowledged. Any opinions, findings, and conclusions or recommendations expressed in this paper are those of the authors and do not necessarily reflect the views or policies of the National Science Foundation.

Data availability

Some or all data, models, or code that support the findings of this study are available from the corresponding author upon reasonable request.

References

[1] Bridgman PW. Studies in large plastic flow and fracture: with special emphasis on the effects of hydrostatic pressure. Harvard University Press; 1964.

[2] McClintock, A Criterion for ductile fracture by the growth of holes, J Appl Mech, ASME Series E 35, 1968, 363-371.

[3] Rice JR, Tracey DM. On the ductile enlargement of voids in triaxial stress fields. J Mech Phys Solids 1969;17(3):201–17.

[4] Kanvinde AM, Deierlein GG. A cyclic void growth model to assess ductile fracture in structural steels due to ultra low cycle fatigue. J Eng Mechanics, ASCE 2007;133 (6):701–12.

[5] Kanvinde AM, Deierlein GG. The void growth model and the stress modified critical strain model to predict ductile fracture in structural steels. J Struct Eng, ASCE 2006;132(12):1907–18.

[6] Anderson TL. Fracture Mechanics. 2nd Ed. Boca Raton, FL: CRC Press; 1995.

[7] Besson J, Moinereau D, Steglich D, editors. Local approach to fracture, Euromech-Mecamat 2006, 9th European Mechanics of Materials Conference, Moret-sur-Loing, 9-12 May, 2006; 2006.

[8] Gurson AL. Continuum Theory of ductile rupture by void nucleation and growth: Part I - Yield Criteria and flow rules for porous ductile media. J Eng Mater Technol 1977;99:2–15.

[9] Hancock JW, Mackenzie AC. On the mechanics of ductile failure in high-strength steel subjected to multi-axial stress-states. J Mech Phys Solids 1976;24(3):147–69.

[10] Rousselier G. Ductile fracture models and their potential in local approach of fracture. Nucl Eng Des 1987;105(1):113–20.

[11] Kiran R, Khandelwal K. Fast-to-computer weakly coupled ductile fracture model for structural steels. J Struct Eng, ASCE 2014;140(6).

[12] Wen H, Mahmoud H. New model for ductile fracture of metal alloys. II: Reverse loading. J Eng Mech, American Society of Civil Engineers 2016;142(2):04015089.

[13] Norris Jr DM, Reaugh JE, Moran B, Quinones DF. A plastic-strain, mean stress criterion for ductile fracture. J Eng Mater Technol 1978;100(3):279–86.

[14] Panontin TL, Sheppard SD. The relationship between constraint and ductile fracture initiation as defined by micromechanical analyses. Fracture Mechanics: 26th Volume. ASTM STP 1256; 1995.

[15] Smith C, Kanvinde A, Deierlein G. A local criterion for ductile fracture under low-triaxiality axisymmetric stress states. Eng Fract Mech 2017;169:321–35.

[16] Suresh S. Fatigue of materials. 2nd ed. Cambridge University Press; 1998.

[17] Myers AT, Kanvinde AM, Deierlein GG, Baker JW. A probabilistic formulation of the cyclic void growth model to predict ultra low cycle fatigue in structural steel. J Eng Mech, ASCE 2014. https://doi.org/10.1061/(ASCE)EM.1943-7889.0000728, 04014028.

[18] Bao Y. Prediction of ductile crack formation in uncracked bodies. Ph.D. dissertation. Cambridge, MA: Massachusetts Institute of Technology; 2003.

[19] Seidt JD. Plastic deformation and ductile fracture of 2024–T351 aluminum under various loading conditions. Ph.D. dissertation. Corvallis, OR: Oregon State Univ; 2010.

[20] Gao X, Zhang T, Hayden M, Roe C. Effects of the stress state on plasticity and ductile failure of an aluminum 5083 alloy. Int J Plast 2009;25(12):2366–82.

[21] Barsoum I, Faleskog J. Rupture mechanisms in combined tension and shear—Experiments. Int J Solids Struct 2007;44(6):1768–86.

[22] Wierzbicki T, Bao Y, Bai Y. A new experimental technique for constructing a fracture envelope of metals under multi-axial loading. Proc., 2005 SEM Annual Conf. and Exposition on Experimental and Applied Mechanics; 2005a. 1295–1303.

[23] Bai Y, Teng X, Wierzbicki T. On the application of stress triaxiality formula for plane strain fracture testing. J Eng Mater Technol 2009;131(2):021002.

[24] Bai Y. Effect of loading history in necking and fracture. Ph.D. dissertation. Cambridge, MA: Massachusetts Institute of Technology; 2008.

[25] Dunand M, Mohr D. On the predictive capabilities of the shear modified Gurson and the modified Mohr-Coulomb fracture models over a wide range of stress triaxialities and Lode angles. J Mech Phys Solids 2011;59(7):1374–94.

[26] Bai Y. Fracture of 1045 steel under complex loading history. Proc., Numisheet 2011, Seoul, Korea; 2011.

[27] Bao Y, Treitler R. Ductile crack formation on notched Al2024-T351 bars under compression-tension loading. Mater Sci Eng A 2004;384(1):385–94.

[28] Wen H, Mahmoud H. New model for ductile fracture of metal alloys. I: monotonic loading. J Eng Mech, Am Soc Civil Eng 2016;142(2):04015088.

[29] Bao Y, Wierzbicki T. On fracture locus in the equivalent strain and stress triaxiality space. Int J Mech Sci 2004;46(1):81–98.

[30] Xiang P, Jia LJ, Shi M, Wu M. Ultra-low cycle fatigue life of aluminum alloy and its prediction using monotonic tension test results. Eng Fract Mech 2017;186:449–65.

[31] Jia L, Kuwamura H. Ductile fracture model for structural steel under cyclic large strain loading. J Constr Steel Res, Elsevier 2015;106:110–21.

[32] Huang X, Zhao J. A cumulative damage model for extremely low cycle fatigue cracking in steel structure. Struct Eng Mech, TechnoPress 2017;62(2):225–36.

[33] Kermajani M, Malek-Ghaini F, Miresmaeili R, Baghi-abadi MK, Mousavi-nasab M. Damage mechanisms in the ultra low cycle fatigue loading. Eng Fract Mech Elsevier 2020;223:106772.

[34] Xue L. A unified expression for low-cycle fatigue and extremely low cycle fatigue and its implication for monotonic loading. Int J Fatigue, Elsevier 2008;30:1691–8.

[35] Pereira JCR, de Jesus AMP, Fernandes AA. Ultra-low cycle behaviour of a structural steel. Eng Struct 2014;60:214–22.

[36] Martinez X, Oller S, Barbu LG, Barbat AH, de Jesus AMP. Analysis of ultra low cycle fatigue problems with the Barcelona plastic damage model and a new isotropic hardening law. Int J Fatigue, Elsevier 2015;73:132–42.

[37] Webb GI. Overfitting. In: Sammut C, Webb GI, editors. Encyclopedia of Machine Learning. Boston, MA: Springer; 2011.

[38] Cooke RJ. Micro-mechanical simulation of ductile fracture processes in structural steel". Doctoral Dissertation. University of California Davis; 2015.

[39] Smith CM, Deierlein GG, Kanvinde AM. A stress-weighted damage model for ductile fracture initiation in structural steel under cyclic loading and generalized stress states. TR 187, Blume Earthquake Engineering Center, Stanford University; 2014.

[40] Johnson GR, Cook WH. Fracture characteristics of three metals subjected to various strain, strain rates, temperatures, and pressures. Eng Fract Mech 1985;21(1):31–48.

[41] Terashima M, Deierlein GG. Ductile fracture simulation and risk quantification of buckling-restrained braces under earthquakes. TR 206, Blume Earthquake Engineering Center, Stanford University; 2020.

[42] Hibbitt D, Karlsson B, Sorensen P. Abaqus/CAE user's guide, ABAQUS 6.11, Dassault Systèmes Simulia Corp., Providence, RI; 2013.

[43] Armstrong PJ, Frederick CO. A Mathematical Representation of the Multiaxial Bauschinger Effect. Berkeley, UK: Berkeley Nuclear Laboratories, Research & Development Dept; 1966.

[44] Smith CM, Kanvinde AM, Deierlein GG. Calibration of continuum cyclic constitutive models for structural steel using Particle Swarm Optimization. J Eng Mech, ASCE 2017;143(5):04017012.

[45] Pericoli VS, Kanvinde AM. Theoretical study of ductile fracture in steel structures in the presence of spatial variability in toughness. J Struct Eng, Am Soc Civil Eng 2018;144(5):04018024.